








Open Archive Toulouse Archive Ouverte (OATAO)

OATAO is an open access repository that collects the work of Toulouse researchers and makes it freely available over the web where possible

This is an author's version published in: <http://oatao.univ-toulouse.fr/24391>



Official URL: <https://doi.org/10.1111/jace.16809>

To cite this version:

Boloré, Damien and Gibilaro, Mathieu  and Massot, Laurent  and Chamelot, Pierre  and Cid, Emmanuel  and Masbernat, Olivier  and Pigeonneau, Franck *X-ray imaging of a high-temperature furnace applied to glass melting.* (2019) *Journal of the American Ceramic Society.* 1-14. ISSN 0002-7820

Any correspondence concerning this service should be sent to the repository administrator: tech-oatao@listes-diff.inp-toulouse.fr

X-ray imaging of a high-temperature furnace applied to glass melting

Damien Boloré¹ | Mathieu Gibilaro² | Laurent Massot² | Pierre Chamelot² | Emmanuel Cid²  | Olivier Masbernat² | Franck Pigeonneau³ 

¹UMR 125 CNRS/Saint-Gobain, Surface du Verre et Interfaces, Aubervilliers Cedex, France

²Laboratoire de Génie Chimique, Université de Toulouse, CNRS, INPT, UPS, Toulouse, France

³MINES ParisTech, PSL Research University, CEMEF – Centre for Material Forming CNRS UMR 7635, Sophia Antipolis Cedex, France

Correspondence

Franck Pigeonneau, MINES ParisTech, PSL Research University, CEMEF—Centre for Material Forming, CNRS UMR 7635, CS 10207, Claude Daunesse 06904 Sophia Antipolis Cedex, France.

Email: franck.pigeonneau@mines-paristech.fr

Present address

Damien Boloré, SEFPRO – Saint-Gobain Research North America, 9 Goddard Rd, Northborough, MA 01532, USA

Abstract

The dynamics of soda-lime-silica glass grain melting is investigated experimentally using a nonintrusive technique. A cylindrical alumina crucible is filled with glass cullet and placed into a furnace illuminated by an X-ray source. This glass granular bed is gradually heated up to 1100°C, leading to its melting and the generation of a size-distributed population of bubbles rising in the molten glass. An image processing algorithm of X-ray images of the cullet bed during melting allows the characterization of bubbles size distribution in the crucible as well as their velocity. The introduction of tin dioxide μ -particles in the glass matrix before melting enhances the texture of the images and makes possible the determination of the bubble-induced molten glass velocity field by an optical flow technique. The bubble size distribution can be fitted by a log-normal law, suggesting that it is closely related to the initial size distribution in the cullet bed. The liquid motion induced by the bubbles in Stokes' regime is strongly affected by the flow confinement and the determination of bubble rising velocity along its trajectory unveils the existence of local tiny temperature fluctuations in the crucible. Overall, the measuring techniques developed in this work seem to be very promising for the improvement of models and optimization of industrial glass furnaces.

KEYWORDS

bubbles, glass melting, optical flow, two-phase flow, X-ray imaging

1 | INTRODUCTION

Glass melting is one of the most difficult industrial processes to study due to various physical, chemical, thermal, and multiphase flow phenomena involved during the batch-to-liquid conversion.¹ Direct observations inside a furnace or introduction of measurement sensors also lead to important experimental difficulties due to a very aggressive environment. For instance, the measurement of the glass velocity in a real plant is an important issue. In order to study the glass melting process, physical (experimental) models using scaled systems with “model” liquids can be employed. In parallel, numerical

simulations based on first principles are increasingly used.² However, experimental data in molten glass are still needed to validate these models and improve the accuracy of computation fluid dynamics (CFD) tools.

Greene and Gaffney³ were among the first to investigate in situ observations for monitoring the glass melting process. They studied the shrinkage of O₂ bubbles. To set a bubble in the field of view, the apparatus designed by these authors applied a rotation to the crucible. They determined the temporal behavior of O₂ bubbles and estimated the diffusion coefficient of oxygen.⁴ High-temperature observation with laboratory furnaces has been developed by Němec⁵ to study

TABLE 1 Suppliers and purity of raw materials to melt the glass with a chemical composition given in Table 2

Raw materials	Supplier	Purity
Roncevaux sand	Samin	≥ 99.6 wt% in SiO_2
Sodium carbonate	Novacarb	≥ 99.9 wt% in Na_2CO_3
Limestone	Samin	≥ 99.5 wt% in CaCO_3
Sodium sulfate	Prolabo	≥ 99.5 wt% in Na_2SO_4
Tin dioxide	Merck	≥ 99 wt% in SnO_2

the fining process with bubbles in motion in silica crucibles. Nowadays this technique is a common tool used by various groups working in glass science as on glass foaming,⁶ bubble shrinkage⁷ or bubble nucleation.⁸

Due to multiple interfaces, the in situ monitoring of raw materials or cullet melting is not achievable with a visible light camera. X-ray imaging is a powerful tool to follow various phases by different absorption contrasts without scattering. For instance, the dynamics of the batch-to-glass melting process has been studied with in situ high-temperature X-ray tomography in a synchrotron facility.⁹ This technique allows real-time observation of chemical reactions occurring between grains of raw materials, which is a noticeable breakthrough of this decade. Unfortunately, this technique is still limited to microscopic samples. Consequently, the large surface-to-volume ratio screens out bulk transformations. At a centimeter scale, the X-ray technique working with a moderate power of X-ray source has been used for nondestructive investigations of a liquid fed ceramic melter.¹⁰ Even more recently, X-ray imaging has been used for studying the melting behavior of borosilicate waste glasses.¹¹

In this article, an X-ray technique coupled with a high-temperature furnace has been employed to follow the melting of different glass granular media. Recently, Boloré and Pigeonneau¹² showed that a large population of bubbles can be created during the melting of recycled glasses. With a high-temperature furnace and charge-coupled device (CCD) cameras with flat samples, they observed bubble nucleation right on the interfaces between the recycled glass and silica crucible. The X-ray system developed and presented in this paper aims at investigating the same phenomenon for dispersed grain cullet. Despite the use of other X-ray imaging in previous contributions mentioned above, studies focusing on the hydrodynamics are scarce. Our purpose here is to go further by developing adequate image analysis. First, size distributions of gas inclusions as a function of grain size are determined to characterize the bubble population. The second

objective is to learn about the multiphase fluid dynamics using an original optical flow technique.

In the following, materials and methods are first detailed, including glass synthesis. Since the main purpose of the experimental setup is to measure the velocity field in a glass-forming melt induced by a population of bubbles rising in the crucible, image analysis, and optical flow methods are also detailed in Section 2. Section 3 is devoted to results on bubble size distributions, velocity field of glass-forming melt and bubble rising velocity.

2 | MATERIALS AND METHODS

2.1 | Materials

The glass has been synthesized with raw materials given in Table 1. Raw materials have been manually weighed and mixed. To estimate the liquid velocity field, small-oxide particles have been dispersed in the glass matrix as flow tracers. These particles are designed to absorb the X-ray light and enhance the contrast and have been chosen considering two constraints. Their X-ray absorption must be higher than that of molten glass, leading to consider heavy and/or dense oxides. Moreover, these particles should not dissolve in molten glass. Solid particles of SnO_2 have been selected due to their very slow dissolution in the glass. Then bubble formation in contact between molten glass and SnO_2 particles was not observed during experiments. However, these bubbles could exist but due to the relatively low spatial resolution of the imaging system, these inclusions were not detected. Finally, for the present purpose, the influence of the particles on the oxidation state of the glass could be neglected. Even if present, it would not have affected the bubble growth rate.

Before melting, the batch is homogenized in a three-dimensional mixer Turbula® for 15 minutes. The batch is then introduced several times into a platinum crucible of 400 cm³ electrically heated at approximately 1475°C. Once melted, the glass is mechanically stirred with a platinum stick for 1 hour and then left at high temperature for 2 hours. Thus, it is ensured that the refining is complete and that the glass only contains a small number of residual bubbles. Just before casting the glass on a cast iron plate, 1 wt % (ie, 0.34 vol%) of SnO_2 particles are introduced and dispersed in the glass with a platinum stick. Particle size ranges between 160 and 200 μm . Once the glass is poured onto a plate, it is immediately annealed in a furnace at 550°C for 1 hour, and then allowed to cool slowly. The chemical composition is given in Table 2 which is close to a composition of window glass.

Once the glass plate is cold, two types of samples have been prepared. First, glass cylinders of 19 mm in diameter (to fit the crucible internal diameter) and approximately 30 mm in height are made. To produce the second kind of samples, the glass plate is broken and introduced into a

TABLE 2 Chemical composition (wt%) of the glass used for experiments

SiO ₂	Na ₂ O	CaO	Al ₂ O ₃	K ₂ O	SO ₂	Fe ₂ O ₃	FeO
73.10	12.75	11.40	1.77	0.74	0.15	0.02	0.0054

crusher, resulting in glass grains. Due to the large dispersion in size, glass grains are sorted by sieving through four different sizes equal to 315 μm , 0.8 mm, 2 mm, and 8 mm. Grains less than 315 μm in size are spheroidal while grains larger than 8 mm in size have complex shapes and have the appearance of gravel.

Following the glass composition given in Table 2, the density is calculated according to the statistical model of Fluegel et al.¹³ At 1100°C, the density is equal to 2383 kg/m³ with a confidence level of 95%. The surface tension is important to estimate the influence of the capillary force in comparison to gravity force. It is also computed with a statistical model according to Kucuk et al.¹⁴ The surface tension is equal to 0.315 N/m at $T = 1400^\circ\text{C}$. Since the surface tension does not change strongly with the temperature,¹⁵ the previous value is used to estimate the surface tension at $T = 1130^\circ\text{C}$ which is the nominal temperature of the furnace, see the next subsection. The dynamic viscosity is measured with a high-temperature viscometer. Data fit very well with the Vogel-Fulcher-Tammann law¹⁵ chap. 3 written as follows:

$$\mu = \mu_0 \exp\left(\frac{B}{T - T_0}\right), \quad (1)$$

with $\mu_0 = 7.29 \times 10^{-2}$ Pa s, $B = 4425$ K, $T_0 = 890$ K, and T in K. At $T = 1130^\circ\text{C}$, the dynamic viscosity of the molten glass is equal to 405.3 Pa s.

2.2 | Experimental setup

The X-ray source is a YXLON power generator of 2250 W. The voltage can rise to 160 kV, and the intensity is set equal to 11.25 mA. The generator is connected to a cooling system. The X-ray source can be seen like a point source and the beam has a maximum angle of 30°. The dose rate is $22 \times 10^9 \mu\text{Sv h}^{-1}$ at 10 cm from the source, which is far beyond standards in amplitude for an uncontrolled and unsupervised zone (below 80 $\mu\text{Sv h}^{-1}$). Consequently, the zone is considered red monitored zone and no one can approach the device while operating. A complete lead shielding of the room is therefore necessary (between 8 and 10 mm thick) to ensure that outside doses are compatible with the standards. The generator is connected to a computer outside the lead bunker. All these protections allow the control desk to be in an unsupervised and uncontrolled area.

To measure the transmitted intensity, a flat panel of 200 mm \times 200 mm with 1024 px \times 1024 px is used. The conversion of X-ray is direct. Images are recorded on 14 bits in direct view. The image recording is done using the software

provided by TCG Air Company. The acquisition frequency can vary between 0.5 and 100 Hz.

A stepper motor allows turning the crucible around the vertical axis as shown in Figure 1. The angular velocity is set to $2\phi \text{ rad s}^{-1}$ (360° s^{-1}) and the motion is paused every rotation of $\pi/2$ (90°). The integration of the X-ray signal is inverse to the frequency acquisition of 15 images/s. Successive images are systematically acquired at each rotation of $\pi/2$ during several complete rotations and stored for processing.

The furnace is supplied by AET Technologies and operates at a nominal temperature of 1100°C. A thermal homogeneity assessment has been carried out with a thermocouple introduced in the furnace at different locations and setpoint temperatures. The thermal homogeneity at the crucible location is good, that is, within 5°C. The temperature in the furnace is underestimated by the setpoint temperature. This difference is equal to 30°C at the setpoint temperature of 1100°C. Such a difference must be accounted for in the computation of the glass viscosity, which drastically varies in this range of temperature. The glass sample described in Section 2.1, is introduced into an alumina crucible (AL23) manufactured by Umicore. The crucible is circular with an exterior and interior radii, respectively, equal to 12.5 and 9.5 mm and a 20 cm height. The overall spatial resolution of the apparatus is about 80 $\mu\text{m}/\text{px}$. Bubbles nucleated at the molten glass-alumina interface are not observed because of their small size.

The geometry of the experimental setup is shown in Figure 1. The spatial resolution reached by the device is mainly determined by the distances between the X-ray source, the sample, and the flat panel. As it is shown in Figure 1, the distance between the X-ray generator and the crucible L_{up} is equal to 46 cm, and the distance between the crucible and the flat panel L_{down} is equal at 98 cm. Unfortunately, it is not possible to reduce the distance between the crucible and the generator. The flat panel is set as far as possible to get the largest amplitude.

Consider a bubble of radius a placed on the axis between the X-ray generator and the flat panel as in Figure 2. Let a' the projected radius of the bubble in the flat panel. The application of the Thales's theorem gives:

$$\frac{a'}{a} = \frac{L_{\text{up}} + L_{\text{down}}}{L_{\text{up}}} \simeq 3.13, \quad (2)$$

where L_{up} and L_{down} are defined in Figure 1.

The error on the radius induced by the position of a bubble in the crucible can be estimated. This error is not fundamental if the crucible is rotating but it gives a good idea of the angles and uncertainties. Consider the same bubble located

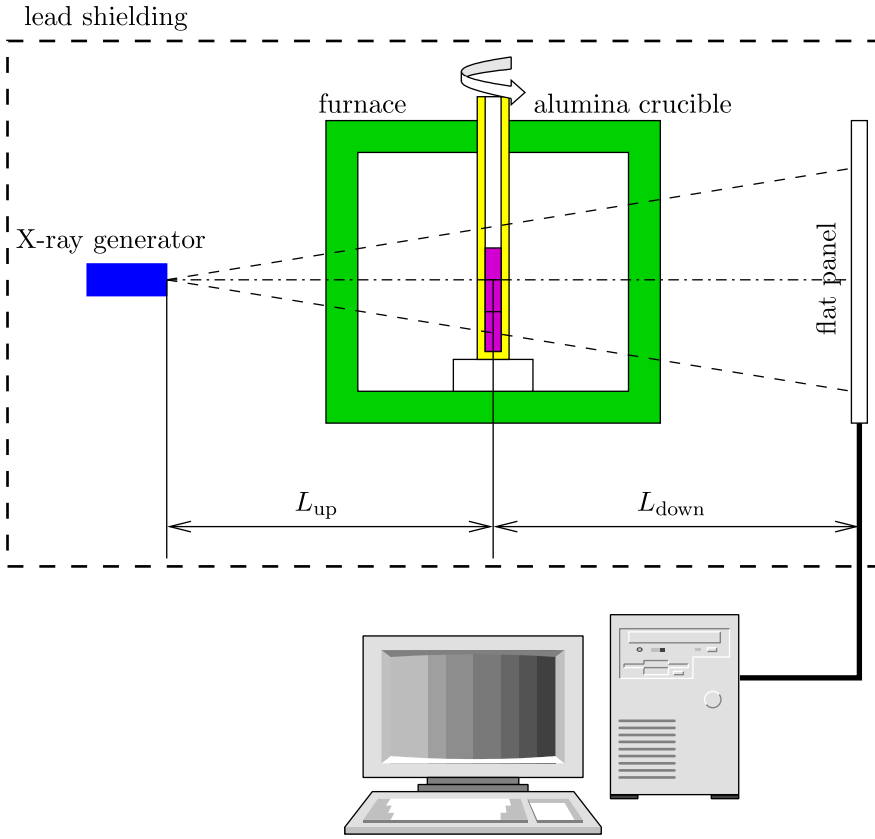


FIGURE 1 Sketch of the experimental setup with the X-ray source on the left, the furnace in the middle, and the flat panel on the right. The alumina crucible is circular and can rotate around its revolution axis

rather upstream or downstream of the crucible, as shown in Figure 2.

In the upstream case, when the real radius is set equal to 2.5 mm and when the bubble is the closest of the crucible, the ratio between the measured and the real radius is

$$\frac{a'}{a} = \frac{L_{up} + L_{down}}{L_{up} - e} \simeq 3.18, \quad (3)$$

while in the downstream case, this ratio is

$$\frac{a'}{a} = \frac{L_{up} + L_{down}}{L_{up} + e} \simeq 3.08. \quad (4)$$

The difference between the two values gives that the position of the bubble can induce a maximum error of 5% which is comparable image processing errors. Indeed, the error on the determination of the radius of small bubbles by image processing can be estimated to 5% for bubble images of a dozen pixels size and with a limited signal-to-noise ratio. These estimations are formally true as long as the detected bubble lies right in the plane perpendicular to the flat panel and centered on the X-ray generator as shown in Figure 2. However, if a bubble is outside this plane, the deviation angles are never large (4° at most) leading to errors of same order of magnitude as those generated along the axis.

The dynamics of the system is driven by the rising velocity of a bubble given by:

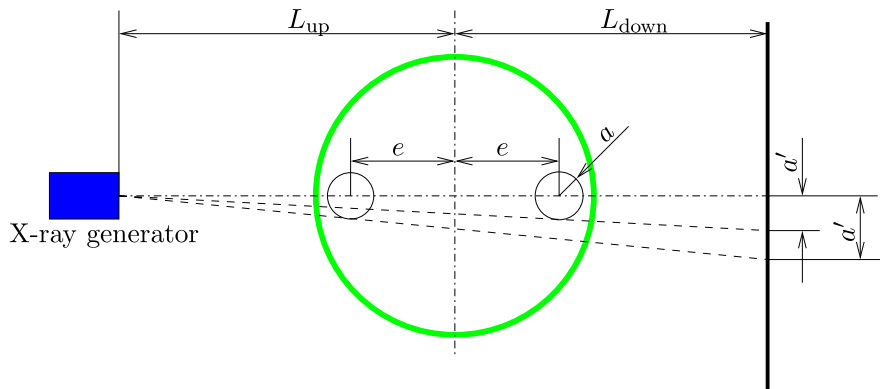


FIGURE 2 Image of a bubble as a function of its position in the crucible

$$V_{H-R} = \frac{\rho g a^2}{3\mu}, \quad (5)$$

in the Stokes regime where ρ is the liquid density, g the gravity acceleration, a the bubble radius, and μ the dynamic viscosity of the liquid. This velocity is given for an infinite domain using the Hadamard-Rybczynski drag law.^{16,17} The studied bubbles always had a radius less than or equal to 2.5 mm so the maximum of rising velocity in a molten glass at 1130°C is of the order of 0.12 mm s⁻¹. The maximum distance traveled by a bubble between two acquisitions at the same angle (separated by 32 seconds) is therefore of the order of 3 mm, that is, a bubble radius. This distance is small enough for the algorithm presented below to follow the bubble between two successive images.

To account for the interaction with the wall, the bubble position in the crucible needs to be accurately known. The uncertainty about the bubble position is definitively removed using two perpendicular views as illustrated in Figure 3. From these two pictures, the wall interaction is clearly evidenced. For the particular snapshot depicted in Figure 3, a 5-mm bubble near the bottom of the crucible is attached to the wall of the crucible.

2.3 | Image analysis

Although crucibles were chosen as straight as possible, a rotation of 90° causes a slight visible change in the orientation of the crucible around its axis of revolution. A sorting algorithm of images as a function of the angular position of the

crucible was therefore required. First, two consecutive images at the same angle change only by the small variations of location of bubbles and liquid motions enabling the allocation of each image to a given angular position of the crucible. Then, it is necessary to perform image registration to a common reference frame to remove the change in position of the crucible due to its rotation. An algorithm developed under the Matlab environment and based on a B-spline grid-based registration was used for this purpose.^{18,19} This algorithm can be decomposed as follows:

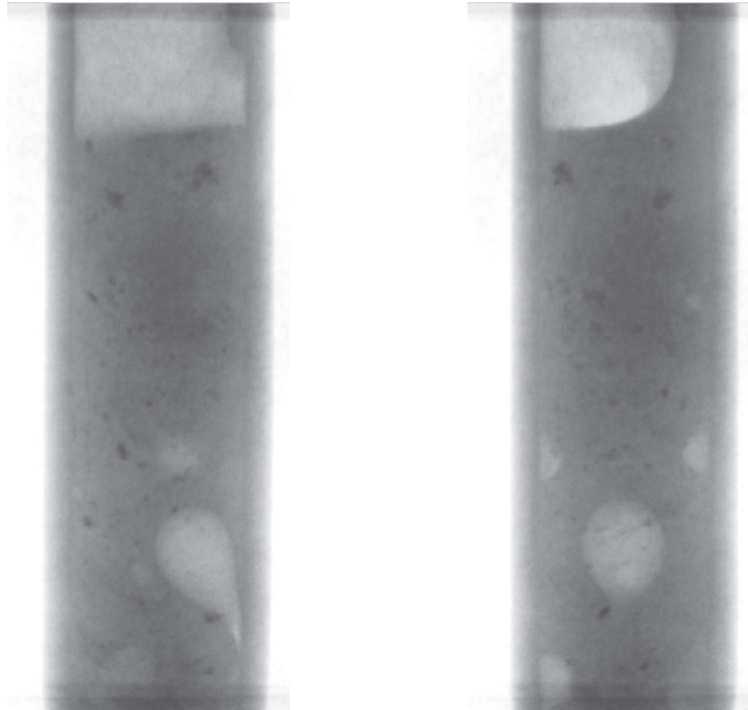
1. Record of an image at a reference position (position of the crucible before rotation);
2. Record of a second image at another angle (after rotation of 90°);
3. Determination of the matrix transform between the two images with an image registration algorithm;
4. Registering the moving image to the reference image.

A solid body displacement is chosen to reorient the crucible without local transformations of the liquid and the bubbles which would degrade the accuracy of the subsequent computations. Figure 4 shows pictures obtained with the algorithm applied to a relevant example similar to the snapshot of Figure 3. In this particular case, a bubble that is stacked on the wall can be tracked in a three-dimensional reference frame. Figure 4D provides the positions of objects from two points of view.

The images obtained by the X-ray device are strongly driven by X-ray absorption. A dark pixel corresponds to a strong absorption while a light pixel to a weak absorption.

FIGURE 3 Images of a crucible with molten glass at the nominal temperature, $T = 1130^\circ\text{C}$ with bubbles: (A) before rotation and (B) after a rotation of 90°

(A) Crucible image without rotation (B) Crucible image after a rotation of 90°



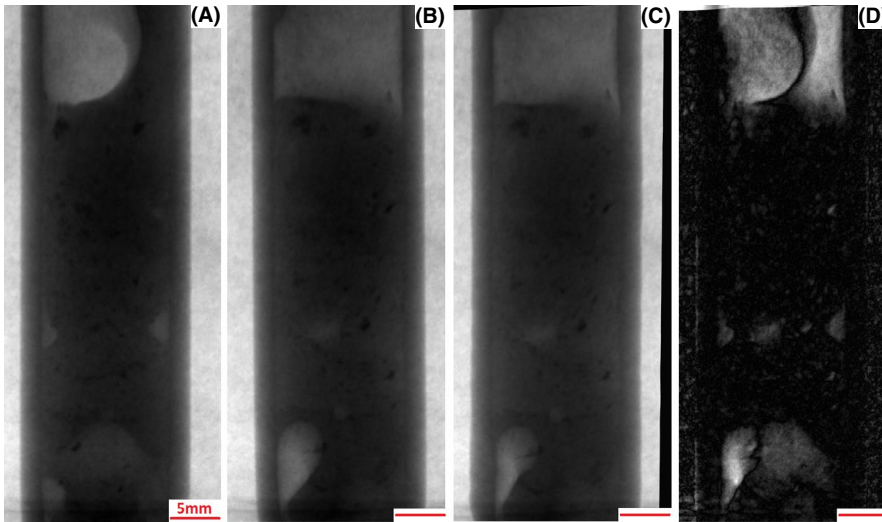


FIGURE 4 Sequence of image analysis: (A) picture of reference without rotation, (B) picture obtained after a rotation of 90°, (C) registered moving image from the picture given in (B), (D) Absolute value of the difference between the reference image and registered moving image (only bubbles remain visible)

As shown in Figures 3–5, the center of the crucible is darker than the periphery because the thickness of material to cross is larger in the middle of the crucible than on the periphery. To overcome these variations, the minimum gray level corresponding to the maximum absorption is computed for every pixel on each image acquired over a complete sequence. This minimum is then subtracted from all images removing all fixed objects from the current image. Figure 5 provides the successive processing steps from the original snapshot recorded by the X-ray imaging given in Figure 5A. The image obtained after this first step is depicted in Figure 5B showing the enhancement of the global contrast.

In a second step, quasi-immobile objects are filtered out applying a sliding local minimum operation over a series of 10 consecutive images (separated by 0.067 seconds). This

operation increases the contrast of higher dynamics objects. It can be observed in Figure 5C that the small bubbles disappear because they do not move over the 10 images sequence. This is the major interest of the seeding and the oxide particles moving under the effect of the bubble motion induce a texture effect clearly visible in Figure 5C around the largest bubble. This contrast-enhanced image is used to determine the velocity field shown in Figure 5D using a technique detailed in the next subsection.

2.4 | Velocimetry by optical flow technique

An optical flow algorithm developed by Sun et al²⁰ has been implemented to measure the liquid motion. Optical flow is often compared to particle image velocimetry (PIV) since it

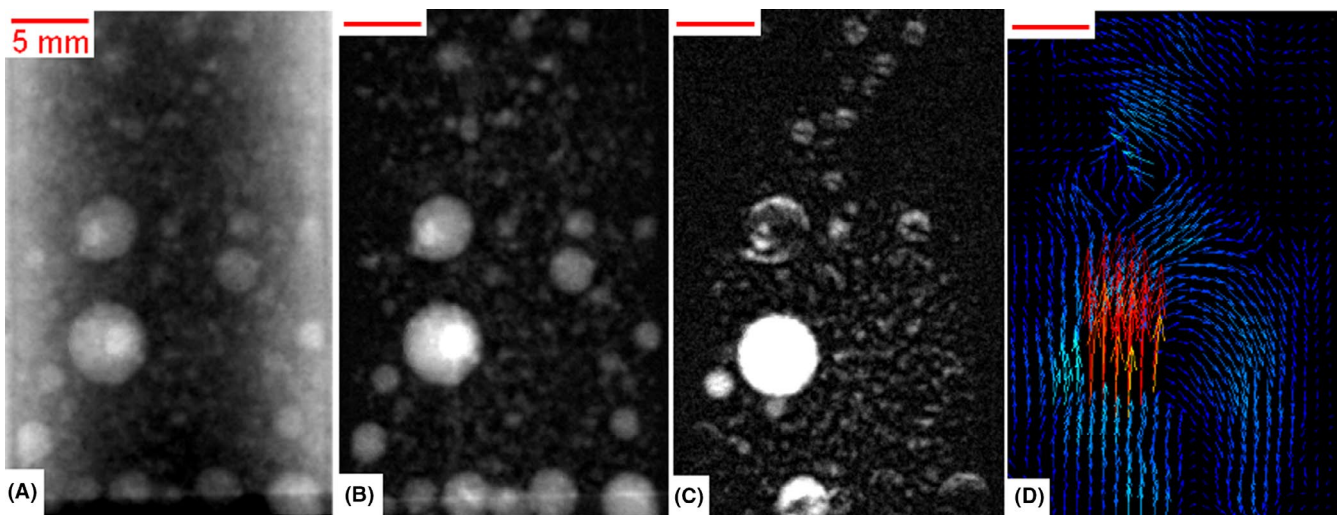


FIGURE 5 Images of a same snapshot after two main operations: (A) original image, (B) subtraction of the overall minimum of the entire sequence, (C) subtracting of the sliding minimum on a sequence of 10 frames, and (D) Vector field resulting from the calculation of the optical flow

gives access to the same quantities. PIV is an optical technique which consists in measuring the displacement of μ -particles seeding the fluid and scattering the light of a laser source illuminating the flow. The instantaneous fluid velocity field is then calculated from the autocorrelation function of particle grey level between two successive images of the flow.²¹

The optical flow technique determines the velocity field by a different method. It is based on the calculation of motion of intensity patterns between two successive frames. The principle has hardly changed since the major contribution of Horn and Schunck²² even if since then algorithms have been substantially optimized.

Several assumptions are made to determine the velocity field. One requires a quasi-uniform lighting. It is also needed that the transmitted light is continuous and smooth in space and time, which is generally the case. Each pixel is associated with an image intensity denoted I which depends on the two Cartesian coordinates x , y , and time t . If this object moves, the intensity is conserved:

$$I(\Phi(\mathbf{X}, t), t) = I_0(\mathbf{X}), \quad (6)$$

where $\Phi(\mathbf{X}, t)$ is the mapping or motion law function between the Lagrangian and Eulerian configurations. The Lagrangian coordinates \mathbf{X} define the position of a material point in a reference configuration while the Eulerian coordinates given by $x = \Phi(\mathbf{X}, t)$ correspond to the position of the same material point in the configuration at time t .²³ Differentiating the former equation with respect to t results in the transport equation:

$$\frac{\partial I}{\partial t} + \frac{\partial I}{\partial x} \frac{D\Phi_x}{Dt} + \frac{\partial I}{\partial y} \frac{D\Phi_y}{Dt} = 0, \quad (7)$$

in which the operator D/Dt is the material derivative and (Φ_x, Φ_y) are the Cartesian coordinate components of Φ . By introducing the Eulerian velocity components as follows:

$$U_x = \frac{D\Phi_x}{Dt}, \quad (8)$$

$$U_y = \frac{D\Phi_y}{Dt}, \quad (9)$$

Equation (7) becomes

$$\varepsilon_b = \frac{\partial I}{\partial t} + \mathbf{U} \cdot \nabla I. \quad (10)$$

The principle of the optical flow is to minimize the previous equation to determine the two velocity components, U_x and U_y . However, Equation (10) cannot be solved with two unknowns without introducing additional assumptions. A classical hypothesis is to consider that the velocity at a

given point is close to the velocity in its neighborhood, which means that the velocity field is regular. This assumption can be written by minimizing the velocity difference in each point to its immediate neighborhood:

$$\varepsilon_c^2 = (U_x - \bar{U}_x)^2 + (U_y - \bar{U}_y)^2, \quad (11)$$

in which \bar{U}_x and \bar{U}_y are the average of velocity components in the neighborhood of the considered point.

Finally, the optical flow amounts are computed by minimizing the sum of errors of Equations (10) and (11). As a general rule, the error ε_c is multiplied by a hyperparameter as a weighting factor of this regularization term. Horn and Schunck²² advise to set its value nearly equal to the noise on the norm of the intensity gradient.

In practice, the optical flow algorithm takes two successive images and returns the horizontal and vertical velocity field over the entire image. It is then possible to exploit these velocity fields to facilitate the image segmentation. Figure 5D results from the application of the algorithm of the optical flow. The arrows represent the direction of the velocity and the color their magnitude which will be quantified in more details in Section 3.3. Note, however, that X-ray recorded images are projections of objects distributed in the entire sample volume and not in a plane section of this sample, limiting the range of the present method to the study of highly dilute bubbly flows.

3 | RESULTS AND DISCUSSION

3.1 | Overall melting dynamics

For each experiment, glass cullet of grain size is introduced into an alumina crucible at room temperature before heating the furnace at a 12 K/min heating rate. The maximum of the furnace temperature is set to 1100°C. However, as already mentioned in Section 2.2, the real temperature of the glass sample is 1130°C.

Cullet is a granular medium with a large grain size range and different grain shapes. Such medium is far from models discussed in the literature on granular media generally focused on mono- or bidisperse media. Recently, Zhao et al²⁴ consider numerically random granular medium stacks for polydisperse granular media. They show that the apparent density of media and the average number of contacts between grains depends strongly on the polydispersity. As a reminder, in the case of a stack of monodisperse spheres, the random close packing is equal to 0.64 and the average number of contacts is 6.²⁵ For grains of more complex shapes, the solid volume fraction average is 0.7 and the average number of contacts can vary between 8 and 9.

Figure 6 displays six snapshots of the crucible during the heating stage at different times and temperatures. Starting

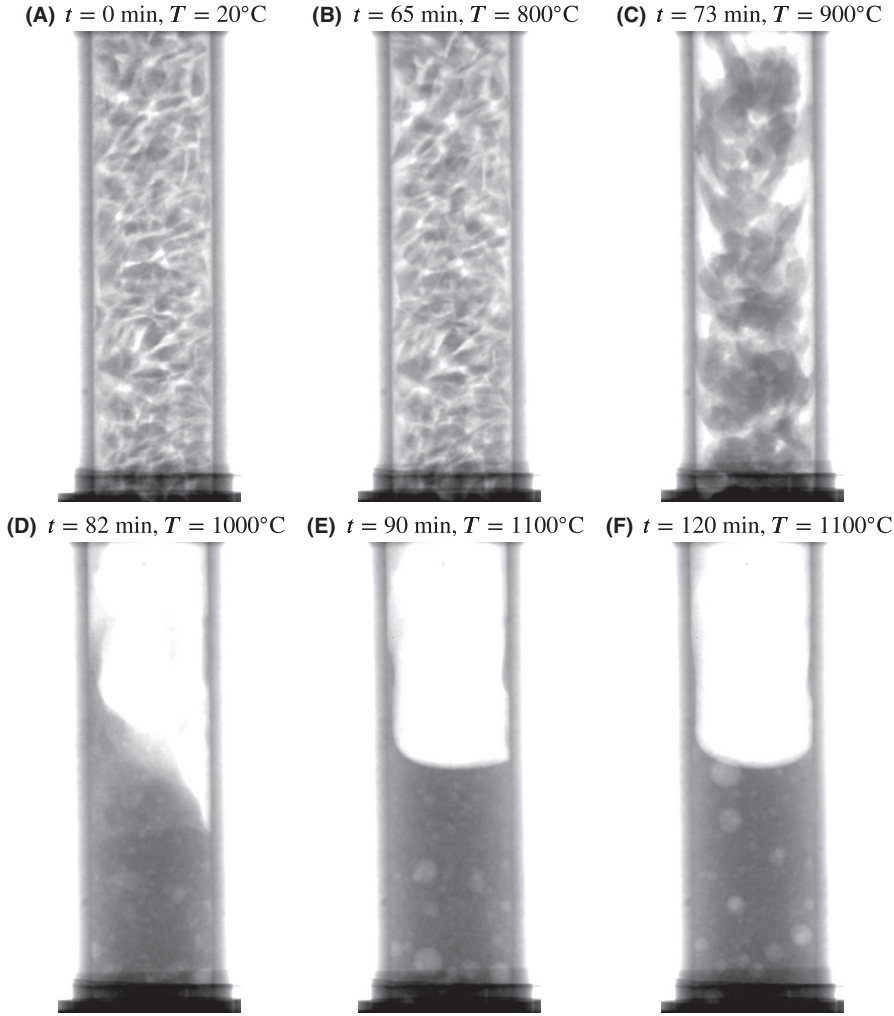


FIGURE 6 Snapshots of the melting a glass granular medium with coarse grain size (6-8 mm) from the room temperature to 1100°C with a heating rate of 12 K/min. In each snapshot, T corresponds to the temperature recorded by the working panel of the furnace

from glass particles in the initial condition shown in Figure 6A, the temperature of grains gradually increases at a rate of the order of 12 K/s. At a temperature of 800°C, as shown in Figure 6B, the medium does not evolve significantly while the glass transition has occurred 45 minutes after the start of the heating ($T_g \sim 570^\circ\text{C}$). In the same temperature range, the gas density has been reduced by a factor 3.66 due to thermal dilatation. Consequently, the interstitial gas is easily released from the granular medium because the porosity stays open and the permeability is large. The Carman-Kozeny relation²⁶ provides an estimation of the permeability around $7 \times 10^{-8} \text{ m}^2$ for the larger grain and $3.5 \times 10^{-10} \text{ m}^2$ for the smaller.

During the downflow, a large amount of gas releases from the granular medium. Initially, the granular medium in the crucible fills the whole crucible. After the melting, the volume occupied by the liquid decreases roughly by a factor two meaning that the initial solid volume fraction can be estimated equal to 50% which is far from the solid volume fraction of 70% given in the reference.²⁴ The cullet is not fully compacted explaining the difference. Indeed, during the filling of the crucible at room

temperature, the friction between the crucible and grains reduces strongly the solid volume fraction. Only a small amount of gas is trapped during the melting. Bubbles with a typical radius around 2.5 mm are created as it is shown in Figure 6E,F. Finally, under the gravity force, these bubbles rise in the crucible and break after reaching the free surface.

It is noteworthy that the glass-forming melt wets the crucible with a small contact angle. This observation can be a result of the large difference in surface energies between alumina and molten glass. Indeed, according to Kingery,²⁷ the alumina-gas surface energy is around $\gamma_{\text{sg}} = 0.9 \text{ J/m}^2$. Using in first approximation, the additivity law of Fowkes,²⁸ the surface energy between alumina and the glass-forming melt can be estimated at around $\gamma_{\text{sl}} = 0.15 \text{ J/m}^2$. Consequently, the spreading coefficient defined by de Gennes²⁹:

$$S = \gamma_{\text{sg}} - (\gamma_{\text{sl}} + \gamma), \quad (12)$$

is positive meaning that the spreading is fulfilled.

The collapse of the granular bed starts at $T = 900^\circ\text{C}$ (Figure 6C) and ends 9 minutes later (Figure 6D). The

shrinking of the glass grains is a competition between gravity and viscous forces when filling the interstitial volume with the molten glass. The time scale of this collapse can be seen as the time for a bubble generated by the interstitial volume to rise in the molten glass over a characteristic distance of the bed structure. For a regular cubic arrangement (which is consistent with the experimental bed porosity), it can be shown that this distance is of the order of the grain size L , as well as the diameter of the interstitial bubble. So at first approximation, the bubble velocity can be estimated with Equation (5), $\rho g L^2 / 12 \mu$, and the time of collapse of the bed is of the order of $12 \mu / \rho g L$. As the molten glass viscosity μ is a strong decaying function of temperature in this temperature range (cf Equation 1), the bubble is substantially accelerated while rising. Taking a constant heating rate of 12 K/min, the distance traveled by the bubble reaches the grain size (6-8 mm) after a time of 9-10 minutes, which nicely compares with the experimental observation. From a process viewpoint, the knowledge of this characteristic time is important regarding the optimization of cullet granulometry and heat power in glass furnaces.

3.2 | Bubble size distributions

The bubble size distribution drives the dynamics of a two-phase molten glass. The size distribution of bubbles has been measured after the bed had collapsed ($T = 1100^\circ\text{C}$). The produced bubbles are closely related to the initial bed structure and during the melting process. Also, the heat transfer in a packed bed of grains combines thermal conduction, convection, and radiative transfer,³⁰ the contribution of each depends on porosity, interfacial area and shape of the grains. As an example, heat transfer is probably enhanced by the number of contacts per grain.

Figure 7 displays the evolution of bed structure during melting for three different cullet grain sizes and shapes. Images in the first column show the granular medium at room temperature. The central column represents the state of the medium at the onset of collapse and the last column are images of the resulting molten glass observed at 1100°C . Rows (a), (b), and (c) respectively correspond to large (6-8 mm), medium (2-3 mm), and small (300-800 μm) grain sizes. The melting of large grains (6-8 mm) results in a vertical down-flow and the entrapment of large bubbles of same order of magnitude as the grain size and few smaller ones. For smaller grains (300-800 μm), the number of smaller bubbles with a size of few millimeters or below increases significantly. Qualitatively, the interstitial volume between the finer grains is initially smaller than for a larger grain size so the gas inclusions follow the same trend.

The crucible wall plays a key role in the overall melting dynamics which can be considered as a limitation of the experimental setup. Indeed, the down-flow leads to a liquid motion

along the wall with a possible entrapment of gas inclusions. For that reason, only bubbles close to the center of the crucible have been taken into account in the measurement of size distribution in order to reduce the influence of this near-wall flow.

Figure 8 shows the distribution of bubble radius for three grain sizes. Note however that the size spectrum of the bubbles is limited by the spatial resolution of the X-ray imaging system (80 μm) excluding bubbles with a radius smaller than 50 μm . Depending on the grain size, between 50 and 200 bubbles have been manually processed in the volume of the crucible (25 cm^3). As expected, the finer grain bed (300-800 μm) provides the smaller bubbles and the narrower distribution. For the larger grain, the distribution is spread over a larger size range. As shown in Figure 8, the experimental probability density functions are very well matched by a log-normal distribution given by

$$f(a, \zeta, \sigma) = \frac{1}{a\sigma\sqrt{2\pi}} \exp\left[-\frac{(\ln a - \ln \zeta)^2}{2\sigma^2}\right], \quad (13)$$

in which a is the bubble radius. Values of the two parameters ζ and σ obtained by the nonlinear regression are reported for the three grain sizes in Table 3. It is noteworthy that the first parameter ζ corresponds to the median of the bubble radius distribution.³¹ The mean radius $\langle a \rangle$ is given by $\zeta \exp(\sigma^2/2)$ and has been also reported in Table 3. Between the finest and the largest grain sizes, the average bubble size is multiplied by a factor 2.65.

The log-normal size distribution is characteristic of various processes of generation of dispersed phases like for instance emulsification or atomization. Rajagopal³² proved that the existence of the law (Equation 13) assuming that the generation of a dispersed phase is mainly due to random processes produced for instance by turbulent phenomena. Using the central limit theorem,³³ Rajagopal demonstrated first that the stochastic process is a Markoff chain and that the probability distribution function converges at long time toward the log-normal distribution. Another explanation of the log-normal distribution proposed by Cramer³³ is based on the joint effect of a large number of mutually independent causes, as occurring for instance in biological phenomena. In the present case, the generation of bubble size distribution is probably closely connected to the initial structure of the voids in the granular bed as studied by Reboul et al³⁴ for a random packed bed of polydispersed spheres. The log-normal bubble size distribution has been used to initialize the bubble size distribution in CFD modeling of bubble dynamics in a glass furnace.³⁵

3.3 | Velocity field by the optical flow technique

Characterization of the velocity field in a glass-forming melt containing a single bubble has been achieved using optical

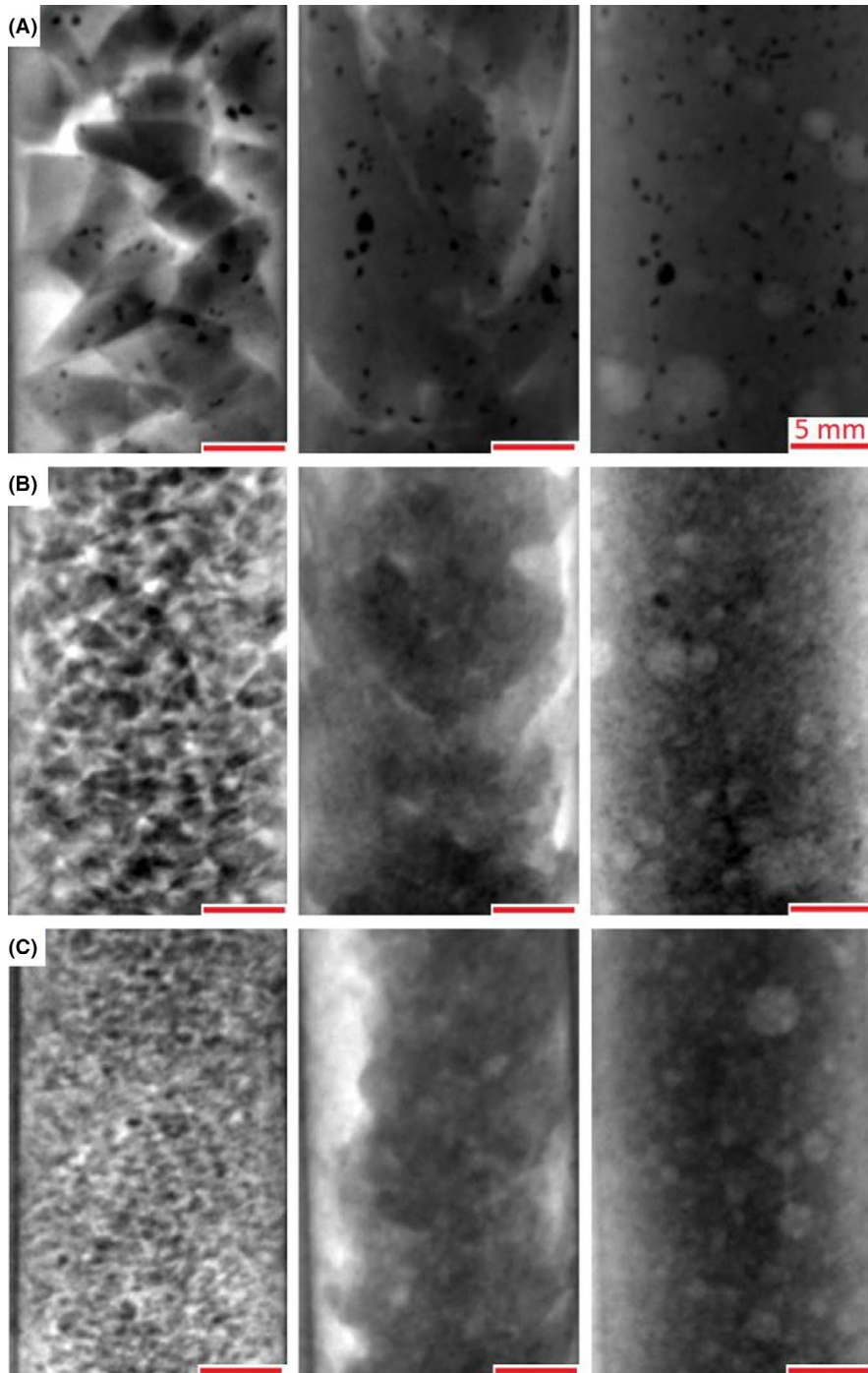


FIGURE 7 Snapshots before melting (1st column), at the beginning of down-flow (2nd column), and in liquid state (3rd column) for (A) coarse grain size, (B) medium grain size, and (C) small grain size

flow technique. In that aim, two identical glass solid cylinders with a hollow asperity on their tip have been introduced in the crucible as illustrated in Figure 9. The diameter of each cylinder slightly smaller than the crucible diameter and the hollow asperities are facing each other in order to generate a single bubble rising in the center of the crucible once the glass melting has ended.

The surrounding velocity field at several positions of the bubble has been measured with the optical flow technique presented in Section 2.4. An averaged velocity field in the laboratory framework has been determined by re-positioning

the bubble to the middle of the image. Figure 10 illustrates two cases obtained with a bubble radius equal to (a) 2.25 mm and (b) 3.42 mm, after reaching a stable rising velocity. The first image from the left results from the image processing detailed in Section 2.3. The second and third images display the fields of the vertical and horizontal velocity components (in $\mu\text{m/s}$) respectively. Note that these fields have been calculated in the image frame with a vertical axis oriented downward, explaining the negative sign of vertical velocity. The last image is the stream function in the laboratory frame (vertical axis oriented upward).

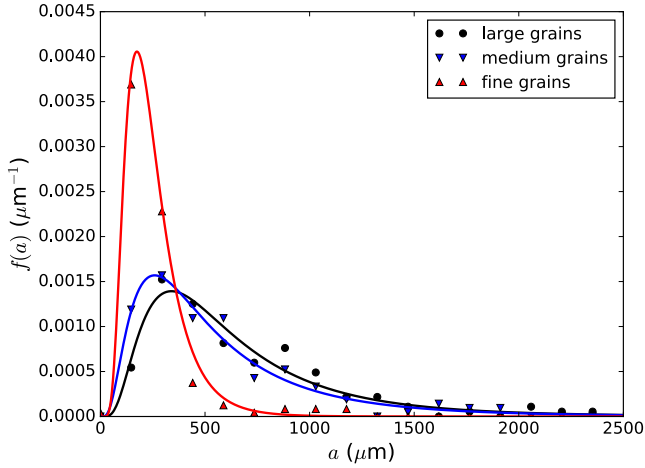


FIGURE 8 Bubble size distributions initially formed after melting for three grain sizes: fine grain (300-800 μm), medium grain (2-3 mm) and large grain (6-8 mm). Solid lines are the bubble size distributions obtained with Equation (13)

TABLE 3 Parameters ζ and σ of the log-normal distribution obtained by a non-linear regression and applied to the experimental data for the three grain sizes. The last column corresponds to the mean radius

Grain size	ζ (μm)	σ (-)	$\langle a \rangle$ (μm)
Fine	223.48	0.4981	253.00
Medium	450.77	0.7436	594.32
Large	533.68	0.6731	669.36

As expected, the vertical component is maximum at the rising front of the bubble interface and this velocity corresponds to the bubble velocity. Note that velocity field inside the bubble is a pure artefact since there is no X-ray tracers within the bubble.

The horizontal velocity field exhibits a quadrupole field signature of the momentum source term created by the rising bubble (Stokeslet and point-source dipole).³⁶ Around the bubble, the vertical velocity of the glass-forming melt is positive, exhibiting a recirculation loop. Upstream of the bubble, the liquid is pushed toward the sides of the crucible wall and thus deviates from the trajectory of the bubble.

From the vertical and horizontal velocity fields, the flow streamlines have been plot in Figure 10. In both cases, a recirculation loop attached to the bubble is observed, due to the presence of walls, with a well-marked asymmetry. This asymmetry probably results from the visible offset of the bubble position with respect to the center of the crucible.

3.4 | Bubble rising velocity

Bubble center of mass has been tracked over time to determine its velocity. Due to the high value of the molten glass

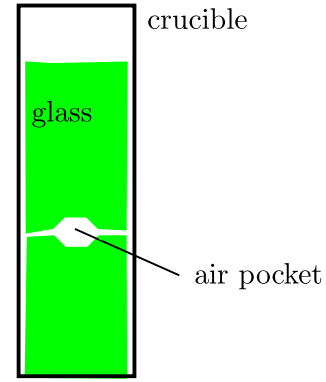


FIGURE 9 Introduction of two glass cylinders to form a single bubble in the center of the crucible

viscosity at 1130°C (~ 400 Pa s), Reynolds number of millimeter size bubbles is very small ($< 10^{-7}$) and liquid velocity around a rising bubble is solution of the Stokes equations of motion. In this regime, the liquid velocity perturbation in the frame of reference of the bubble is inversely proportional to the distance from the bubble center.³⁷ In such a confined flow as that considered in this study, the hydrodynamic interactions with the crucible wall are not negligible. The terminal velocity of a spherical fluid inclusion rising in a liquid along the axis of a circular tube has been theoretically investigated by Haberman and Sayre³⁸ in Stokes' regime. The drag force is a function of the ratio $\lambda = ar$ (with a and r being, respectively, the radius of the fluid inclusion and of the tube) and of the viscosity ratio between the two fluids. In the present case, it reads:

$$F = 4\pi\mu aVK(\lambda), \quad (14)$$

in which V is the bubble velocity and $K(\lambda)$ is the wall correction factor taking the following form for a bubble:

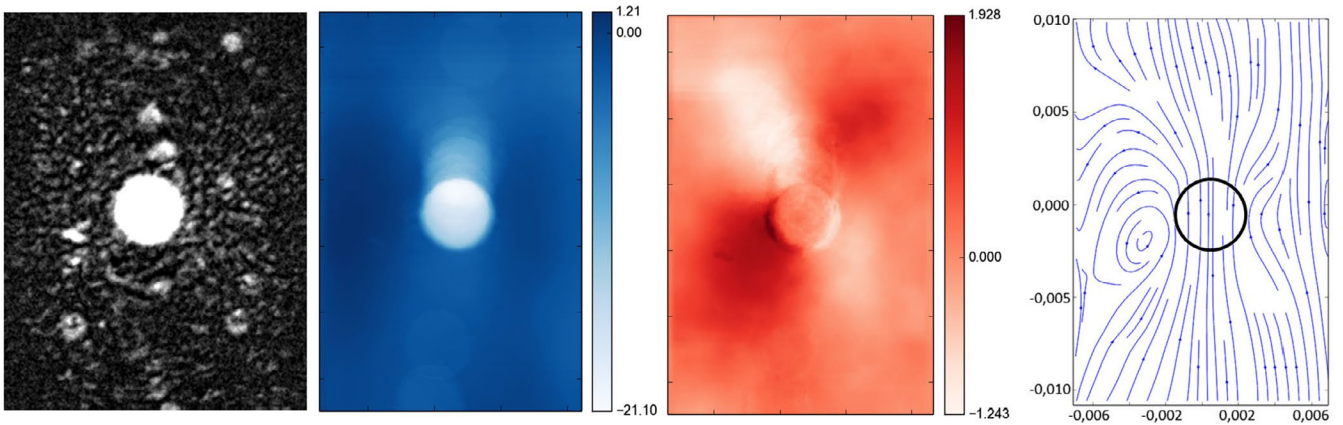
$$K(\lambda) = \frac{1 + 1.137855\lambda^5}{1 - 1.4033\lambda + 1.13787\lambda^5 - 0.72603\lambda^6}. \quad (15)$$

Balancing drag and buoyancy forces, the ratio between the terminal rising velocity in a tube and that in an infinite domain (Equation 5) is given by:

$$\frac{V}{V_{H-R}} = \frac{1}{K(\lambda)}. \quad (16)$$

Black curves in Figure 11 show the evolution of this velocity ratio as a function of the normalized vertical distance in the crucible ($z = 0$ corresponds to the initial position of the bubble at the end of the melting phase) for two experiments performed with the same bubble size ($a \sim 2$ mm and $\lambda \simeq 0.2$). As expected, the ratio is smaller than unity but larger than the theoretical value predicted by (Equation 16), which is equal to 0.73 for this bubble size. In both

(A) Bubble with $a = 2.25$ mm



(B) Bubble with $a = 3.42$ mm

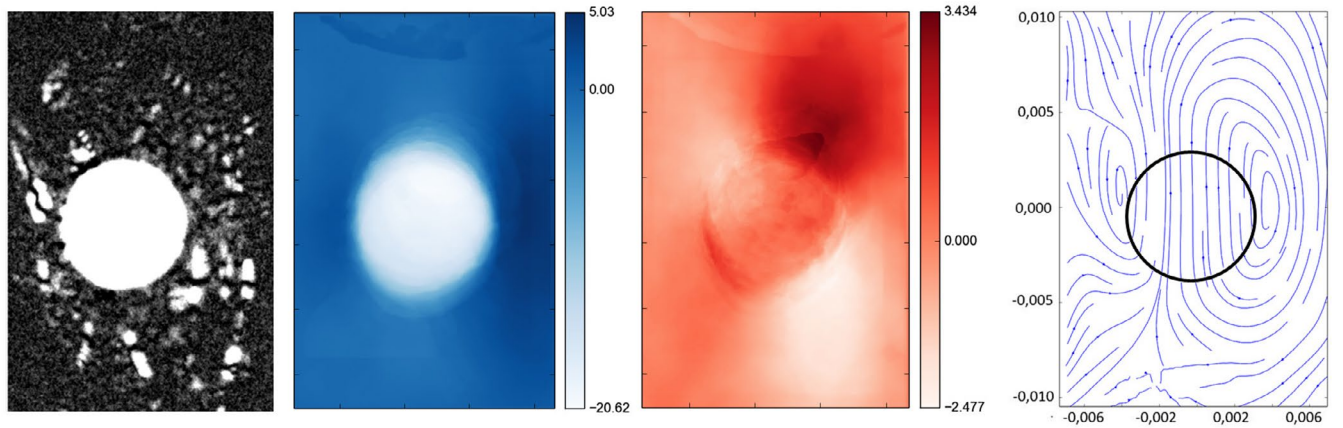


FIGURE 10 Image with recalibration around a rising bubble for two bubble sizes. The second and the third images are the vertical and horizontal velocity fields obtained by the optical flow technique in $\mu\text{m/s}$. The right figure is the stream function

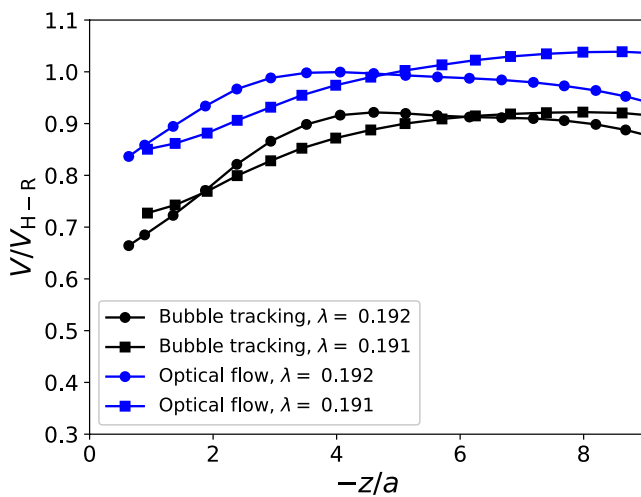


FIGURE 11 Bubble reduced velocity as a function of travelled distance in the crucible for two experiments with $a = 2$ mm. Comparison between trajectography (black symbols) and optical flow (blue symbols) measurements

cases, the bubble is first accelerated over a distance of the order of twice its diameter, then tends toward a plateau or slightly decreases when approaching the free surface. This length of acceleration does not correspond to the dynamic response of a bubble in molten glass: the characteristic time of the bubble ($\rho a^2/[6\mu K(\lambda)]$) is less than $10 \mu\text{s}$, so the bubble reaches its terminal velocity instantaneously, suggesting that the variations observed during its trajectory are likely to result from local temperature fluctuations in the crucible. At 1100°C , a 1% temperature variation ($\sim 10^\circ\text{C}$) induces a variation on the viscosity larger than 20%, and so a variation of same order of magnitude on the velocity in Stokes' regime. This fluctuation level compares with the difference between the experimental ($K^{-1} \sim 0.9$) and theoretical ($K^{-1} \sim 0.73$) values of the velocity ratio in the plateau region of Figure 11. This acceleration region is observed for all different bubbles tested, suggesting the development of a positive temperature gradient upstream of the bubble that could result from the interaction between the bubble and the molten glass in the heat transfer balance. Near the

top of the crucible, the bubble slowdown may also be due to the hydrodynamic interaction between the bubble and the free surface.^{39,40}

The same experiments were also processed by the optical flow algorithm previously used to characterize the liquid flow field. Instantaneous bubble velocity was computed using the velocity vectors at the interface. The blue curves of Figure 11 represent the axial profile of the bubble velocity determined with this method for the same bubbles. The shape of these curves is highly similar to those calculated from classical trajectography, but they are overestimating the trajectography data (supposed to best represent the actual bubble velocity) by a nearly constant offset of 10%. The origin of this offset might be due to the fact that the optical flow algorithm is applied on X-ray projections of the bubble rising-induced flow. On these projected images, several processing steps have been applied in order to enhance the contrast. Combination of the projection and of the image processing probably favors the larger dynamics objects, resulting in the observed overestimation. Note also that if, as suggested, temperature fluctuations are present, the velocity scaling as $1/\mu$, larger velocities are likely to be more weighted on projected images. Even if the offset seems to be constant, its correction needs complementary investigations.

4 | CONCLUSION

In this work, the complex flow dynamics generated in a crucible by the melting of a bed of cullet grains at 1130°C has been investigated using X-ray imaging. The recording of projected images of the medium allows the visualization of the collapse of the cullet bed, the bubble generation, their motion and the molten glass hydrodynamics. Bubble size distributions have been characterized for three contrasted size ranges of cullet grain. For all grain sizes, it is found that a log-normal distribution provides a good approximation of bubble size experimental data, as a result of the initial size distribution of voids in the cullet bed prior to the melting. This result is important regarding the modeling of industrial furnaces when coupling CFD and population balance models.

When the glass is fully melted, the bubbles are tracked individually. In order to characterize the liquid hydrodynamics generated by these bubbles, glass samples containing small SnO₂ particles have been synthesized. Using an adequate image processing, the dynamics of texturized patterns on each image by an optical flow algorithm allows the determination of the velocity field in the liquid phase, which is the major contribution of this work. Investigations have been focused on the hydrodynamics created by one bubble artificially introduced in the crucible. As a first result, it is shown that the rising velocities of bubbles cannot be correctly predicted

even by the Hadamard-Rybczynski law when accounting for wall corrections. This anomalous behavior is likely to be due to the presence of temperature heterogeneities in the crucible which induce, in this range of temperature, substantial variations of viscosity, and consequently of bubble velocity in Stokes regime. This result also highlights the importance of accurate temperature field prediction in industrial glass furnaces.

This contribution is the first attempt of measuring molten glass hydrodynamics using X-ray imaging. It can be concluded that X-ray imaging is a powerful tool to analyze the dynamics of molten glass containing dispersed bubbles. However, investigations in that field are still needed to improve the flow measurement method. In particular, the filtering effect due to the projected image and image analysis must be characterized more thoroughly to obtain a better reliability on the velocity field using optical flow technique. Finally, the development of 3D X-ray imaging and tomographical reconstruction algorithms will increase the accuracy of the method.

ORCID

Emmanuel Cid  <https://orcid.org/0000-0003-0564-4596>

Franck Pigeonneau  <https://orcid.org/0000-0003-2184-0378>

REFERENCES

1. Shelby JE. Introduction to glass science and technology. Cambridge: The Royal Society of Chemistry; 2005.
2. Viskanta R. Review of three-dimensional mathematical modeling of glass melting. *J Non-Cryst Solids*. 1994;177:347–62.
3. Greene CH, Gaffney RF. Apparatus for measuring the rate of absorption of a bubble in glass. *J Am Ceram Soc*. 1959;42:271–5.
4. Doremus RH. Diffusion of oxygen from contracting bubbles in molten glass. *J Am Ceram Soc*. 1960;43:655–61.
5. Němec L. The refining of glass melts. *Glass Technol*. 1974;15:153–6.
6. Laimbäck P. Foaming of glass melts. PhD thesis, Technische Universiteit Eindhoven; 1998.
7. Pigeonneau F, Martin D, Mario O. Shrinkage of oxygen bubble rising in a molten glass. *Chem Eng Sci*. 2010;65:3158–68.
8. Vernerová M, Cincibusová P, Kloužk J, Maehara T, Němec L. Method of examination of bubble nucleation in glass melts. *J Non-Cryst Solids*. 2015;411:59–67.
9. Gouillart E, Toplis MJ, Grynberg J, Chopinet M-H, Sondergard E, Salvo L, et al. In situ synchrotron microtomography reveals multiple reaction pathways during soda-lime glass synthesis. *J Am Ceram Soc*. 2012;95(5):1504–7.
10. Watanabe K, Yano T, Takeshita K, Minami K, Ochi E. X-ray CT imaging of vitrified glasses containing simulant radioactive wastes: structure and chemical reactions of glass beads and wastes in the cold cap. *Glass Technol: Eur J Glass Sci Technol Part A*. 2012;53(6):273–8.

11. Harris WH, Guillen DP, Klouzek J, Pokorny R, Yano T, Lee SeungMin, et al. X-ray tomography of feed-to-glass transition of simulated borosilicate waste glasses. *J Am Ceram Soc.* 2017;100(9):3883–94.
12. Boloré D, Pigeonneau F. Spatial distribution of nucleated bubbles in molten glasses undergoing coalescence and growth. *J Am Ceram Soc.* 2018;101(5):1892–905.
13. Fluegel A, Earl DA, Varshneya AK, Seward TP. Density and thermal expansion calculation of silicate glass melts from 1000°C to 1400°C. *Phys Chem Glasses: Eur J Glass Sci Technol B.* 2008;49(5):245–57.
14. Kucuk A, Clare AG, Jones L. An estimation of the surface tension for silicate glass melts at 1400°C using statistical analysis. *Glass Technol.* 1999;40(5):149–53.
15. Glass SH. *Nature, structures and properties.* Berlin: Springer-Verlag; 1990.
16. Hadamard J. Mouvement permanent lent d'une sphère liquide et visqueuse dans un liquide visqueux. *CR Acad Sci Paris.* 1911;152:1735–8.
17. Rybczynski RW. Über die fortschreitende bewegung einer flussingen kugel in einem zaben medium. *Bull de l'Acad des Sci de Cracovie, série A.* 1911;1:40–6.
18. Lee S, Wolberg G, Shin SY. Scattered data interpolation with multi-level B-splines. *IEEE Trans Vis Comput Graph.* 1997;3(3):228–44.
19. Rueckert D, Sonoda LL, Hayes C, Hill D, Leach MO, Hawkes DJ. Nonrigid registration using free-form deformations: application to breast MR images. *IEEE Trans Med Imag.* 1999;18(8):712–21.
20. Sun D, Roth S, Black MJ. Secrets of optical flow estimation and their principles. *Proceeding of IEEE Conference on Computer Vision and Pattern Recognition.* San-Francisco, CA. 2010;2432–9.
21. Raffel M, Willert CE, Scarano F, Kähler CJ, Wereley ST, Kompenhans J. *Particle image velocimetry: a practical guide.* Cham, Switzerland: Springer International Publishing; 2018.
22. Horn B, Schunck BG. Determining optical flow. *Artif Intell.* 1981;17(1–3):185–203.
23. Truesdell C, Toupin RA. The classical field theories. In: Flügge S, editor. *Encyclopedia of physics.* Berlin: Springer-Verlag, 1960; p. 226–793.
24. Zhao S, Zhang N, Zhou X, Zhang L. Particle shape effects on fabric of granular random packing. *Powder Technol.* 2017;310:175–86.
25. Andreotti B, Forterre Y, Pouliquen O. *Granular media: between fluid and solid.* Cambridge, UK: Cambridge University Press; 2013.
26. Nield DA, Bejan A. *Convection in porous media.* New York, NY: Springer-Verlag; 2006.
27. Kingery WD. Metal-ceramic interactions: IV, Absolute measurement of metal-ceramic interfacial energy and the interfacial adsorption of silicon from iron-silicon alloys. *J Am Ceram Soc.* 1954;37(2):42–5.
28. Fowkes FM. Additivity of intermolecular forces at interfaces. I. Determination of the contribution to surface and interfacial tensions of dispersion forces in various liquids. *J Phys Chem.* 1963;67(12):2538–41.
29. De Gennes PG. Wetting: statics and dynamics. *Rev Mod Phys.* 1985;57(3):827–63.
30. Wu H, Gui N, Yang X, Tu J, Jiang S. Numerical simulation of heat transfer in packed pebble beds: CFD-DEM coupled with particle thermal radiation. *Int J Heat Mass Transfer.* 2017;110:393–405.
31. Forbes C, Evans M, Hastings N, Peacock B. *Statistical distributions.* 4th ed. Hoboken, NJ: John Wiley & Sons, Inc.; 2011.
32. Rajagopal ES. Statistical theory of particle size distributions in emulsions and suspensions. *Kolloid Z.* 1959;162(2):85–92.
33. Cramér H. *Mathematical methods of statistics.* Princeton, NJ: Princeton University Press; 1946.
34. Reboul N, Vincens E, Cambou B. A statistical analysis of void size distribution in a simulated narrowly graded packing of spheres. *Granular Matter.* 2008;10(6):457–68.
35. Bensberg A, Breitbach C. Bubble continuum model. In: Varner JR, Seward III TP, Schaeffer HA, editors. *Proceedings of the Advances in Fusion and Processing of Glass III.* Westerville, OH: The American Ceramic Society, 2004; p. 91–8.
36. Pozrikidis C. *Fluid dynamics: theory, computation, and numerical simulation.* 2nd ed. New York, NY: Springer; 2009.
37. Happel J, Brenner H. *Low Reynolds number hydrodynamics.* The Hague: Martinus Nijhoff Publishers; 1983.
38. Haberman WL, Sayre RM. Motion of rigid and fluid spheres in stationary and moving liquids inside cylindrical tubes. *David Taylor Model Basin Report 1143.* U.S. Navy Dept; 1958.
39. Pigeonneau F, Sellier A. Low-Reynolds-Number gravity-driven migration and deformation of bubbles near a free surface. *Phys Fluids.* 2011;23:092102.
40. Kočárková H, Rouyer F, Pigeonneau F. Film drainage of viscous liquid on top of bare bubble: influence of the Bond number. *Phys Fluids.* 2013;25:022105.

How to cite this article: Boloré D, Gibilaro M, Massot L, et al. X-ray imaging of a high-temperature furnace applied to glass melting. *J Am Ceram Soc.* 2019;00:1–14. <https://doi.org/10.1111/jace.16809>